Kinetics of selenite interactions with Boom Clay: adsorption–reduction interplay

ALWINA L. HOVING[1]*, MELANIE A. MÜNCH[1], CHRISTOPHE BRUGGEMAN[2], DIPANJAN BANERJEE[3] & THILO BEHRENDS[1]

[1]*Department of Earth Sciences - Geochemistry, Faculty of Geosciences, Utrecht University, Princetonplein 9, 3584 CC Utrecht, The Netherlands*

[2]*Waste & Disposal Expert Group, Unit R&D Disposal, Belgian Nuclear Research Centre (SCK•CEN), Boeretang 200, B-2400, Mol, Belgium*

[3]*Dutch–Belgian Beamline (DUBBLE), European Synchrotron Radiation Facility – 71, avenue des Martyrs, CS 40220, 38043 Grenoble Cedex 9, France*

T.B., 0000-0002-0728-6545

**Correspondence: A.L.Hoving@uu.nl; alwina.hoving@tno.nl*

Abstract: The speciation of selenium (Se) in clay-rich host rocks is important within the framework of geological disposal of radioactive waste since it affects its migration. Removal of selenite from formation water can be caused by reduction and adsorption. Reduction could potentially be inhibited or delayed by adsorption. Here, the interplay of adsorption and reduction of selenite was investigated in batch experiments with Boom Clay and its separated size fractions. In all experiments, dissolved Se concentrations (Se_{aq}) showed a fast initial decrease that was followed by a slower decline until removal was almost complete. X-ray absorption spectroscopy indicated that adsorption of selenite accounted for the fast removal of Se_{aq} followed by slower selenite reduction. Eventually, almost all solid-bound Se^{IV} became reduced to Se^0 in all experiments. The progress of Se_{aq} removal and Se^{IV} reduction to Se^0 could be described by a kinetic model involving reversible adsorption on clay minerals and reduction by pyrite. This implies that the reduction of selenite to Se^0 is not significantly hindered or delayed by selenite adsorption on clay minerals. Pyrite is probably the most relevant reductant for selenite in Boom Clay, although reduction by Fe^{II} structurally bound in clay minerals might provide an additional pathway for selenite reduction in clay rocks.

Supplementary Material: X-ray diffractograms of separated clay-size, silt-size and total BC material are available as Supplementary Material. Also provided are particle size distributions of all materials and extra information on XANES and EXAFS results, Se concentrations through time for experiments with standard clay minerals and figures of the sensitivity analysis of the kinetic model. The information is available at https://doi.org/10.6084/m9.figshare.c.4363826

At the moment, disposal in deep geological formations is seen as the safest long-term solution for radioactive waste (IAEA 2003; Rempe 2007). Many types of geological formations are being investigated regarding their suitability to host a radioactive waste repository, including granitic rocks, salt rocks and clay formations (IAEA 2003). The geological formation should in a first instance act as a hydraulic barrier to impede convective transport of radionuclides potentially released from the engineered disposal facility. Clay formations have the added benefit that they can also retard radionuclide migration by chemical interaction in the form of adsorption and redox reactions (Yllera De Llano *et al.* 1996; Maes *et al.* 2002; Bruggeman *et al.* 2005; Tsai *et al.* 2009).

The Boom Clay (BC), part of the Rupel Formation, in the Netherlands, is considered as a potential host for radioactive waste repositories in Belgium and the Netherlands (OPERA *et al.* 2011). One of the radionuclides of specific interest for the performance assessment is selenium-79 (^{79}Se). ^{79}Se is present in spent nuclear fuel and in wastes resulting from reprocessing this fuel. It is one of the long-lived fission products with a half-life of 327 kyr (Jörg *et al.* 2010; PTB-Physikalisch-Technische-Bundesanstalt 2010). Since selenium has a tendency to bioaccumulate and has a high potential (radio)toxicity (Hamilton 2004), it is critical that this radionuclide is retained in the deep underground. In its most oxidized forms, 6+ and 4+, selenium forms very soluble oxyanions selenate (SeO_4^{2-}) and selenite (SeO_3^{2-}), respectively. Selenium in its reduced redox states, with a valence of 0, −1 and −2, is expected to form low-solubility phases such as elemental selenium

From: Norris, S., Neeft, E. A. C. & Van Geet, M. (eds) 2019. *Multiple Roles of Clays in Radioactive Waste Confinement*. Geological Society, London, Special Publications, **482**, 225–239.
First published online March 12, 2019, https://doi.org/10.1144/SP482-2018-60

(Se^0) and iron selenides ($FeSe_2$ or FeSe), respectively, in Fe-rich environments (De Cannière *et al.* 2010). In BC, natural selenium is expected to occur associated with pyrite or organic matter or in the remains of calcifying organisms such as coccolithophorids (De Cannière *et al.* 2010).

Selenium can occur in radioactive waste in different redox states (De Cannière *et al.* 2010) and might enter BC in the form of selenate and selenite (Bruggeman *et al.* 2005). In experiments with BC and selenate, no adsorption or reduction was observed and its transport appeared to occur unretarded (Beauwens *et al.* 2005; De Cannière *et al.* 2010). Selenite, on the other hand, did interact with BC (Bruggeman *et al.* 2005; Breynaert *et al.* 2010). Retention of selenite can occur through adsorption on clay minerals (Bar-Yosef & Meek 1987; Goldberg & Glaubig 1988; Bruggeman 2006; Peak *et al.* 2006; Missana *et al.* 2009; Goldberg 2013; Ervanne *et al.* 2016), but also through reduction by various minerals such as pyrite and siderite (e.g. Breynaert *et al.* 2008; Scheinost & Charlet 2008; Kang *et al.* 2011; Badaut *et al.* 2012; Charlet *et al.* 2012). This study focusses on selenite as it can react with BC constituents via adsorption and reduction. To describe and predict selenite migration in radioactive waste disposal the underlying retention mechanisms need to be known. For adsorption on clay minerals, solution concentrations can be described using equilibrium partitioning constants. When reduction is coupled to precipitation, solution concentrations can become solubility limited.

Redox active components present in BC that could play a role in selenite reduction are pyrite (FeS_2) and siderite ($FeCO_3$), and possibly natural organic matter and iron (Fe) on/in clay minerals. Reduction of selenite by pyrite leads to poorly soluble elemental Se^0 (Bruggeman *et al.* 2005; Breynaert *et al.* 2008; Curti *et al.* 2013; Kang *et al.* 2013) or possibly $FeSe_2$ (Charlet *et al.* 2012) and is seen as the main reduction process in BC (Breynaert *et al.* 2010). However siderite and clay minerals containing Fe may also contribute to selenite reduction. Studies on selenite reduction by siderite showed that selenite is slowly reduced to Se^0 (Scheinost & Charlet 2008; Scheinost *et al.* 2008; Badaut *et al.* 2012). Fe^{II} adsorbed on clay minerals is also able to reduce selenite to Se^0 (Charlet *et al.* 2007). Structural Fe^{II} in clay minerals and biotite has also been shown to reduce the radionuclides Tc^{VII} and U^{VI} (Ilton *et al.* 2004; Jaisi *et al.* 2009; Peretyazhko *et al.* 2009) and possibly might provide another pathway for selenite reduction in BC.

The other major retention mechanism of selenite is adsorption on clay minerals via the formation of inner-sphere complexes (Bruggeman 2006; Peak *et al.* 2006). The extent of selenite adsorption has been shown to be independent of the ionic strength of the surrounding solution (Bruggeman 2006; Ervanne *et al.* 2016). Therefore the higher salinity of pore water in Dutch BC compared with Belgian BC should not be of influence to selenite adsorption. Selenite adsorption has been reported to depend on pH, with highest adsorption under acidic conditions and a decrease in adsorption towards more alkaline conditions (Bar-Yosef & Meek 1987; Goldberg & Glaubig 1988; Ervanne *et al.* 2016). pH values measured in BC vary between 7.3 and 8.6 (De Craen *et al.* 2004; Behrends *et al.* 2016), at which K_d values of around 100 ml g^{-1} have been measured for pure Na-smectite and Na-illite (Missana *et al.* 2009).

In BC, adsorption and reduction of selenite might act simultaneously and adsorption might interfere with reduction. Adsorption on clay minerals and organic matter has been shown to hinder reduction of selenite to Se^0 by pyrite (Bruggeman *et al.* 2005). Inhibition or delay was also observed for reduction of Tc^{VII} to Tc^{IV} and U^{VI} to U^{IV} by FeS or FeS_2 in the presence of organic matter (Liu *et al.* 2008; Bruggeman & Maes 2010; Huo *et al.* 2017). Selenite interaction with BC has been investigated previously in Belgian BC (Bruggeman *et al.* 2005; Breynaert *et al.* 2010) and effective removal of dissolved selenite was found, with reduction to Se^0 by pyrite as the dominant mechanism on time scales of a month. However, the pyrite and clay mineral content in the Dutch BC can vary considerably (pyrite, 0–6.94 wt%; 2:1 clay, 7.24–63.13 wt%) (Koenen & Griffioen 2016). Consequently, the potential for selenite reduction by pyrite could also diverge, in particular when adsorption to clay minerals is interfering with the interaction of selenite with pyrite. In this study we therefore investigate the interplay and temporal evolution of adsorption and reduction reactions contributing to selenium immobilization. Three approaches are combined to tackle the problem of distinguishing between the processes of adsorption and reduction: (1) investigating the kinetics of selenium immobilization combined with kinetic modelling; (2) using different size fractions from the BC – the clay fraction contains more clay minerals and, hence, enhanced adsorption is expected, while the silt fraction is enriched in pyrite (Delécaut 2004), which is expected to promote reduction; and (3) applying X-ray absorption spectroscopy (XAS) to characterize solid-bound selenium. Combining these approaches allowed us to delineate the relevance and respective contribution of adsorption and reduction to the retention of selenium in a reducing, clay-rich formation.

Materials and methods

All operations involving BC material were performed under anoxic conditions in a glove box filled with either argon gas or a gas mixture of

95%N_2–5% H_2. Materials used for the experiments were autoclaved (Tuttnauer 3150EL). All solutions were deoxygenized by degassing the hot (85°C) sterilized solution under low pressure (0.2 bar) in the antechamber of the glovebox (30 min).

Sediment material

BC sediments originated from a drilled core taken in 2011 in Zeeland, the Netherlands. Two different parts of this core were available to us, KB103A-ST7 (78.72-79.25 m depth) and KB103-ST5 (75.34–75.89 m depth) (detailed descriptions of location, storage and treatment of the cores can be found in Behrends *et al.* 2016). The cores were sliced inside a glovebox and the slices were sterilized by γ-irradiation (30.6–39.1 kGy, Synergy Health, Ede, Netherlands) to exclude any microbiological influence in the experiments. Reduction in BC is considered abiotic owing to the fine pore space limiting microbial activity (Boivin-Jahns *et al.* 1996). However, upon suspension of BC the space and transport limitations are cleared and microbes can become active (Ortiz *et al.* 2002; Aerts *et al.* 2008; Jacops *et al.* 2015). Since under *in-situ* conditions microbial activity is expected to be of negligible influence, the BC samples were sterilized in this study. Three slices were used for the experiments: sample I (depth, 79.16–79.18 m), sample II (depth, 75.65–75.67 m) and sample III (depth, 75.55–75.65 m).

Size separation of the sediment was achieved by wet sieving, separating the sand-size fraction (mesh size 50 μm), and gravitational sedimentation, separating the clay- and silt-size fractions. For the latter, the clay–silt suspension was deflocculated by ultrasonic treatment, after which it was centrifuged at 484 *g* for 3 min. Subsequently, the clay-size containing supernatant was decanted and saved as the clay fraction. The centrifuge tubes or buckets were refilled with sterile, degassed ultra-pure water (UHQ, 18.2 MΩ cm, Purelab Ultra, Elga), and the sediment was resuspended and centrifuged at 484 ***g*** for 3 min. This cycle was repeated until the supernatants were clear, indicating that all clay-sized particles were removed. The remaining sediment on the bottom of the tube was the silt-size fraction, in the following referred to as Silt. About 5 ml of sterile deoxygenated seawater was added to the suspension containing the clay-size fraction to flocculate the clay minerals. The clay-size fraction, in the following referred to as Clay, was separated from solution by centrifugation at 3200 ***g*** for 15 min.

The sediments were characterized by various analyses, including X-ray diffraction (XRD, Co-source; D2 PHASER from Bruker with a LINXEYE™ detector), scanning electron microscopy imaging (SEM, benchtop SEM, Jeol) and elemental analysis by digestion in a heated mixture of HF, HNO_3 and $HClO_4$ measured by inductively coupled plasma – optical emission spectroscopy (ICP-OES) (Spectro Arcos; Reitz *et al.* 2004) or by total reflection X-ray fluorescence spectroscopy (TXRF, S2 Picofox, Bruker). The relative mineral content was evaluated from the integrated intensity of the respective mineral peaks using the reference intensity rations method in the software program EVA (Diffrac suite, Bruker). Particle size measurements based on static light scattering (Mastersizer S long bed version 2.18, Malvern Instruments Ltd) were performed on sediment suspensions that were treated beforehand in an ultrasonic bath (10 min) and with the addition of *c.* 5 ml/0.3 g peptization solution (0.4 M Na_2CO_3 and 9 mM $Na_4P_2O_7$ decahydrate). Studies comparing particle size distributions obtained by static light scattering (vol%) and by sedimentation methods (wt%) demonstrate that static light scattering yields larger particle radii compared with sedimentation methods for identical suspensions. A limit of <8 μm (vol%) obtained by static light scattering corresponds to a limit of <2 μm (wt %) for sedimentation methods (Konert & Vandenberghe 1997; Ramaswamy & Rao 2006), which is the limit for clay size (international scale, ISO 14688-1:2002). The organic carbon content was determined using an elemental analyser (Fison Instruments, NA 1500 NCS) after removing carbonates by repeated washing with 1 M HCl. To analyse the main Fe-containing redox-active phases, the samples were subjected to a sequential Fe extraction (Claff *et al.* 2010; Hoving *et al.* 2017).

Batch experiments

Batch experiments of BC with selenite were performed using the two size fractions, Clay and Silt, and the Total sample. These sediments were suspended to attain a solid loading of 50 g l^{-1}. For this, sterile, degassed, 1:1 diluted seawater of pH 8.3 was used since pore water in BC from Zeeland has a composition close to that of dilute seawater (Behrends *et al.* 2016). After 7 days of equilibration, glass vials (Chromacol 27 ml clear Crimp Top Headspace Vials) were filled with 20 ml suspension and selenium (stock solution 50 mM $Na_2SeO_3{\cdot}5H_2O$) was added, giving final concentrations of 50, 125 and 150 μM, respectively. In general, selenium concentrations were selected based on selenium/solid ratios used in previous experiments (Bruggeman *et al.* 2005), but also in view of the requirements for analysing Se by X-ray absorption spectroscopy and monitoring selenium concentrations throughout the experiments. The headspace of the vials was flushed with argon to prevent any influence of H_2 from the gas mixture in the glovebox, and the vials were closed with rubber stopper and crimp cap. The vials were put into heat-sealed PPT bags

which were, in turn, packed into heat-sealed Ar-filled PETP/Al/PE bags to ensure the exclusion of atmospheric oxygen during agitation of the suspensions outside the glove box on a shaker. At each time step a set of vials was sacrificed and used for analyses. These were centrifuged at 2800 ***g*** for 7 min and supernatants were decanted and filtered through a 0.2 µm filter (nylon, Mfilter). The solution was drawn off the solids by putting them on a filter (Schleicher & Schuell 589[3], cellulose). Subsamples of the solids were smeared into slits of Teflon^{TR} holders that were specifically made for measurements at the European Synchrotron Radiation Facility (ESRF), Grenoble, France. The slits were closed off with Kapton tape. All solids were stored anoxically at −20°C. For the first two sampling moments, 1 and 3 h, solids were frozen using liquid nitrogen in order to quickly cease redox reactions of selenite with BC. The water content of these samples was a maximum of 30%, leading to, on average, 1% of the total Se^{IV} within the wet sediment pastes originating from dissolved selenite. In the solids collected after 1 h reaction time the dissolved selenium concentrations of the remaining solution were higher and contributed to *c.* 6% of total Se^{IV} in the wet pastes. In the 50 µM Se experiment, procedures were mostly identical; however, instead of small 27 ml vials, larger 100 ml Schott bottles were used from which subsamples were taken at each time step. All experiments were run in duplicate and the corresponding sample codes can be found in Figure 1. Additional to experiments with BC, we conducted batch experiments with 50 µM SeO_3^{2-} and two standard clay minerals, ferruginous smectite (SWa-1, Grant County, Washington, USA; Clay Minerals Society, Chantilly, USA) and Fithian illite (Illinois, USA; Ward's Natural Science Establishment, Rochester, USA.). SWa-1 was used in both its natural (oxidized) state as well as after chemical reduction with dithionite (Hoving *et al.* 2017). The experiments with clay mineral standards in both reduced and oxidized state were performed to complement kinetic data on selenite adsorption in a single mineral system. Since clay minerals in BC are present in a reduced state; the standard clay mineral, which is oxidized in its natural state, was chemically reduced to analyse whether this results in different adsorption behaviour. The experimental procedure of the batch systems was the same as in the experiments with BC.

Sample analyses

Se concentrations in the supernatant were measured by ICP-OES (Spectro Arcos) or TXRF (S2 Picofox, Bruker). For Se speciation, solids were subjected to XAS measurements at BM26A, the Dutch–Belgian Beamline (DUBBLE) at the ESRF (Borsboom *et al.* 1998; Nikitenko *et al.* 2008). For measurements, the holders were installed in a closed-cycle He cryostat at 80 K and XAS measurements were performed in fluorescence mode using the nine-element Ge detector (Ortec). Five pelletized reference materials ($Na_2SeO_3{\cdot}5H_2O$, red Se^0 and grey Se^0, FeSe and $FeSe_2$), were measured in transmission mode. A sixth reference, selenite adsorbed to montmorillonite (IMt-1), was measured in fluorescence mode. Here, 20 ml of 250 µM selenite in 1:1 seawater was equilibrated with 1 g of montmorillonite for 2 days. The sample was afterwards treated in the same way as the BC samples. The energy calibration was performed by assigning an energy of 13 035 eV to the steepest part of the Pb–L_{III} edge. Details about the design of the beamline are described in Nikitenko *et al.* (2008) and Borsboom *et al.* (1998). The Athena software package (Ravel & Newville 2005) was used for merging and normalizing the spectra, removing the background for analysing the extended X-ray fine structures (EXAFS), and performing linear combination fitting. Additionally, an iterative target test factor analysis was performed on the X-ray absorption near edge structure (XANES) and EXAFS

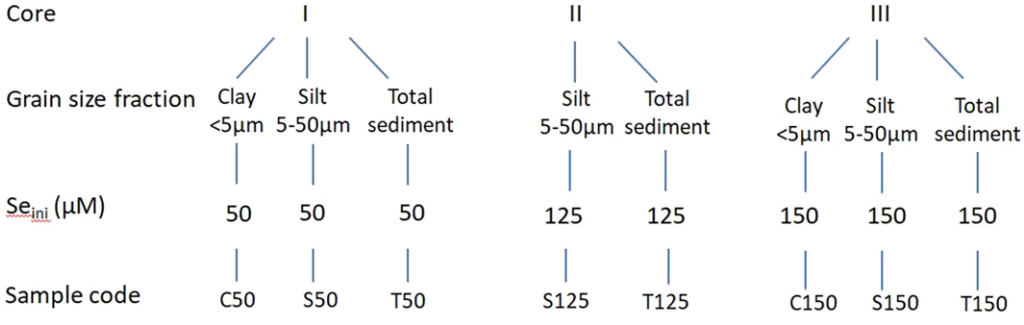

Fig. 1. Sample scheme of batch experiment with BC and its separated grain size fractions with different amounts of Se added.

spectra as an alternative approach to identify and quantify different Se species in the spectra. More details on the reference materials, acquisition of data and analyses of the spectra can be found in the Supplementary Material (S.4). Adsorbed selenium from the experiments with standard clay minerals, SWa-1 and Fithian illite, was extracted by shaking the sediment sample with 0.1 M $NaH_2PO_4{\cdot}H_2O$ for 12 h in a solid solution ratio of 1:25 (Bar-Yosef 1987; Chao & Sanzolone 1989; Dhillon & Dhillon 1999). Se concentrations in the extracts were quantified by TXRF (S2 Picofox, Bruker) with the addition of Ga as internal standard.

Kinetic model

The kinetics of selenite adsorption on clay minerals were modelled by a simple reversible adsorption–desorption model (Zhang & Selim 2005). In this model, the adsorption rate is dependent on the aqueous Se^{IV} (Se^{IV}_{aq}) concentration and the reactive surface area of the clay mineral. The rate of desorption depends on the concentration of Se adsorbed on the clay mineral (Se^{IV}_{ads}).

$$\frac{dSe^{IV}_{ads}}{dt} = k_1 A Se^{IV}_{aq} - k_{-1} Se^{IV}_{ads} \quad (1)$$

In equation (1), k_1 and k_{-1} represent the rate constants of the forward and backward reactions (h^{-1} l m^{-2} and h^{-1}, respectively), A is the reactive surface area of the clay minerals per volume of solution (m^2 l^{-1}) and Se^{IV}_{ads} is the Se concentration of adsorbed Se on the clay (mol l^{-1}).

The reduction of Se^{IV} by pyrite involves multiple steps, but the overall rate is controlled by the electron transfer from pyrite to Se^{IV} (Kang *et al.* 2011). Since the reaction is far from equilibrium, there is no significant back reaction. Therefore an irreversible pseudo first-order rate law is used (equation 2).

$$\frac{dSe^{0}_{pyr}}{dt} = k_2 A Se^{IV}_{aq} \quad (2)$$

where Se^{0}_{pyr} is the concentration of Se reduced by pyrite (mol l^{-1}), k_2 represents the rate constant (l h^{-1} m^{-2}), t is time (h) and A is the reactive surface area of pyrite per solution volume (m^2 l^{-1}). The kinetics of Se^{IV} reaction with pyrite are pH dependent (Kang *et al.* 2011). It is assumed that the pH is constant and hence the reaction constant is conditional for pH around 8.

The time evolution of Se speciation was modelled by simultaneously integrating equations (1) and (2) coupled to the Se mass balance (equation 3) using an numerical (Euler) approach:

$$Se_{tot} = Se^{IV}_{aq}(t) + Se^{0}_{pyr}(t) + Se^{IV}_{ads}(t) \quad (3)$$

Se_{tot} is the total amount of Se in the system (mol l^{-1}). Se^{IV}_{aq} at time 0 h was set at the initial Se concentration of the batch (mol l^{-1}), and Se_{ads} and Se^{0}_{pyr} were assumed to be 0 mol l^{-1} at 0 h. The rate constants k_1, k_{-1} and k_2 were obtained by fitting the model results simultaneously to all experimental BC Se results (Se^{IV}_{ads}, Se^0 from combining XAS and Se_{aq} measurements) using the least squares method. For the surface area of pyrite in BC in equation (2), values from Pugh *et al.* (1981) were used. They measured surface areas for framboidal pyrite, the main form of pyrite in BC (De Craen *et al.* 1998), of 2.3 m^2 g^{-1} for framboids with a mean diameter of 12.5 µm and 4 m^2 g^{-1} for framboids of 2–5 µm. Wei & Osseo-Asare (1997) also found a surface area of 4.1 m^2 g^{-1} for pyrite microcrystalites of 1.5 µm. For the model, the surface area of pyrite in the silt fraction was set to 2.3 m^2 g^{-1} and that of pyrite in the clay fraction and total sample to 4 m^2 g^{-1}. For clay minerals, Se^{IV} sorption takes place on the edges of clay minerals, by exchange of structural OH groups (Bergaya *et al.* 2006; Bruggeman 2006). The BET surface area cannot serve as a proxy for the reactive edge surface area (Metz *et al.* 2005). Here, the clay mineral content in combination with averaged reported values for specific edge surface areas was used to estimate the reactive surface area of the clay minerals (Supplementary Material, Table S.4). Edge surface areas of clay minerals vary from 5.6 ± 0.4 to 29.5 ± 8.7 m^2 g^{-1} for illite (Sayed Hassan *et al.* 2006; Macht *et al.* 2011), from 4.9 ± 0.7 to 15 ± 2 m^2 g^{-1} for smectites (Metz *et al.* 2005; Macht *et al.* 2011) and from 2.5 ± 0.4 to 6.3 ± 3.5 m^2 g^{-1} for kaolinite (Sayed Hassan *et al.* 2006). Two different model scenarios were tested. In the first scenario (M1) both pyrite and clay minerals interact with Se^{IV}_{aq} simultaneously: interaction with pyrite results in Se^0 formation and interaction with clay minerals leads to the formation of Se^{IV}_{ads}. The second scenario (M2) is similar to M1, but includes the possibility of Se^{IV} reduction by clay as an extra reduction step reducing Se^{IV}_{ads} to Se^{0}_{clay}:

$$\frac{dSe^{0}_{clay}}{dt} = k_3 Se^{IV}_{ads} \quad (4)$$

The rate constant for this reduction step (h^{-1}) was obtained by fitting the model results to the experimental BC Se results using the least squares method.

A sensitivity analysis was performed to evaluate potential correlations between model parameters and the time window in which each parameter is important. For this a Monte Carlo simulation using latin hypercube sampling was used. An uncertainty factor of 3 was used around the fitted k-values. In the case of the model including parameter k_3, two sets of calculations were performed, one with a low k_3 value, 10^{-4} h^{-1}, and one with a higher k_3 value of 10^{-3} h^{-1}.

Results and discussion

Characterization of the BC samples and their separated size fractions

Results from particle size analysis, sequential extractions and XRD can be found in Figure 2, Table 1 and the Supplementary Material (S.1 and S.2). The clay-size fraction samples (Clay) consisted predominantly of particles <5 μm with mostly clay minerals (smectite, illite and kaolinite) and minor amounts of quartz and pyrite. The silt-size fraction samples (Silt) contained particles of between 1 and 50 μm with quartz, feldspars, micas (illite or muscovite), pyrite and calcite. The diffractogram of the total sediment (Total) was very similar to that of Silt but with relatively lower feldspar and quartz peaks and slightly broader, more pronounced clay mineral peaks. The content of clay minerals was more than twice as large in Clay samples compared with Silt and Total samples (Fig. 2 and Table 1). Pyrite concentrations were lowest in the Clay samples and were highest in the Silt samples. The Clay samples were enriched in clay minerals but still contained trace amounts of micrometre-sized pyrite particles (SEM imaging, Supplementary Material, Fig. S.3). Iron extracted by 1 M HCl, was also detected in the samples and could represent siderite. However, iron from clay minerals such as chlorite can also dissolve in this extractant, which makes exact determination of the siderite concentrations impossible. Mössbauer spectroscopy analysis from neighbouring samples taken from core part I did reveal the presence of small amounts of siderite (Hoving *et al.* 2017).

Besides mineralogical variation between different size fractions, there were also differences between samples of the same size fraction. For the silt-size fraction, the aluminium content of S125 (core slice II), representing clay minerals and feldspars, was about 2.5 times lower compared with S50 and S150. Pyrite content in samples S125 and T125 (core slice II) was about 2.3 times lower than for samples S50, S150 and T50, T150 (core slices I and III), respectively. Small, centimetre-scale variability of more silty and clayey sediment has been observed in BC cores from Belgium, which can explain the variations in the neighbouring slices observed here.

The organic matter content (C_{org}) of the Total sediment samples was 0.59 wt% C for T50, 0.39 wt% C for T150 and 0.33 wt% C for T125. For the separated size fractions, C_{org} was only measured in the experiment with core slice III. Organic matter was predominantly associated with the clay-size fraction with C150 having 0.89 wt% C_{org}. The silt-size fraction contained 0.41 wt% C_{org}.

Time evolution of aqueous Se

Figure 3 shows the normalized aqueous selenium concentrations (Se_{aq}/Se_{tot}) in the batch experiments

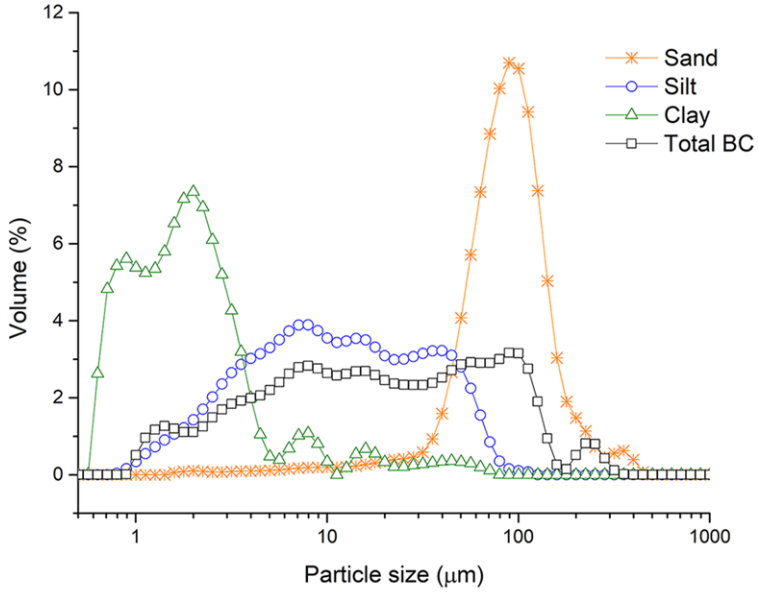

Fig. 2. Particle size distribution of the separated clay, silt and sand fraction and the total sediment of BC core slice III.

Table 1. *Overview of sample characterization by particle size analysis, Fe sequential extraction, elemental analysis (Al), and mineralogical analysis*

Sample	Core	<8 μm*	8–63 μm*	>63 μm*	Fe_{HCl}†	Fe_{HNO3}†	Al‡	Quartz§	Feldspars§	Clay minerals/micas§
		vol%	vol%	vol%	wt%	wt%	wt%	wt%	wt%	wt%
Clay										
C50	I	40	57	3	0.42	0.26	9.6	30	2	60
C125	II	67	23	10	0.68	0.37	8.7	21	1	70
C150	III	94	6	0	0.62	0.36	9.9	12	0	79
Silt										
S50	I	23	72	5	0.28	0.88	8.1	40	19	36
S125	II	25	71	4	0.18	0.37	3.4	54	13	25
S150	III	42	56	0	0.29	0.99	6.4	45	21	28
Total										
T50	I	30	49	21	0.39	0.88	8.2	43	13	36
T125	II	31	41	28	0.26	0.45	6.4	47	14	32
T150	III	32	47	21	0.48	1.14	6.7	44	12	35

*Particle size fractions in volume percentage coinciding with the clay-size fraction (<8 μm), the silt-size fraction (8–63 μm) and the sand-size fraction (>63 μm).
†Fe extracted in a sequential extraction. Fe_{HCL} is Fe^{II} extracted by 1 M HCl (step 2 in Claff *et al.* 2010), which in these samples probably represents Fe from siderite. Fe_{HNO3} is Fe extracted using concentrated HNO_3 (step 5 in Claff *et al.* 2010) and represents Fe from pyrite.
‡Aluminium is measured by ICP-OES in a solution from sediment digested by HF, HNO_3, HCl and $HClO_4$.
§Weight percentages from semi-quantitative analysis of XRD spectra with an error of around 5 wt%.

over time. For all samples, between 10 and 60% of Se_{tot} was removed in the first 3 h, which was followed by a slower, gradual decline. The existence of at least two kinetic stages can be explained by the involvement of two or more processes contributing to Se_{aq} removal. The initial fast removal could be assigned to fast adsorption of selenite while the slower, gradual removal may reflect selenite reduction proceeding with slower kinetics. After 23 days, Se_{aq} concentrations reached steady state. The apparent K_d values for selenium, irrespective of its oxidation state, after 35 days reaction time ranged between 1700 and 9000 ml g^{-1} for Total, between 650 and 2300 ml g^{-1} for Silt and between 2000 and 10 000 ml g^{-1} for Clay. These values exceed by far K_d values reported for selenite adsorption to different types of pure clay minerals at pH 8, which range between 10 and 200 ml g^{-1} (Bruggeman 2006; Missana *et al.* 2009; Ervanne *et al.* 2016). This implies that the removal of Se_{aq} cannot be ascribed solely to selenite adsorption on clay minerals. The steady-state Se_{aq} concentrations for the experiment with Total were between 0.3 and 1.0 μM. These concentrations are comparable with the steady-state Se_{aq} concentration of 0.26 μM found by Bruggeman *et al.* (2005), who performed batch experiments with BC and selenite with the same sediment load but lower selenite concentrations (5 μM). For Silt and Clay the Se_{aq} concentrations at steady state were 1–3 and 0.3–0.5 μM, respectively. The solubility of Se^0 under conditions representative for BC was measured to be between 0.0017 and 0.3 μM (De Cannière *et al.* 2010). Thus, the measured steady-state concentrations exceed the solubility of Se^0. Bruggeman *et al.* (2005) also observed that in BC batch systems a considerable amount of Se_{aq} was associated with dissolved humic substances causing higher Se concentrations in solution. Dissolved organic carbon concentrations, measured in the supernatants of our experiments, were 0.08 g C l^{-1} for Total, 0.20 g C l^{-1} for Silt and 0.36 g C l^{-1} for Clay. The final Se_{aq} concentrations are therefore probably a consequence of substantial reduction of Se^{IV} to Se^0 in combination with equilibrium partitioning of the remaining Se^{IV} between solid and solution and possibly Se associated with dissolved humic substances.

In general Se_{aq} removal proceeded faster in experiments with Clay fraction and Total samples than in experiments with the Silt fraction (Fig. 3). This general trend follows the differences in reactive surface area which is expected to control the rates of heterogeneous reactions. However, the kinetics of Se_{aq} consumption vary considerably between experiments within the same grain size classes. Although these variations in consumption rates might be caused by the differences in initial selenium concentrations, they appear to be more related to mineralogical differences between samples. Samples S50 and S125 exhibit similar consumption rates even though their initial selenium concentrations were almost 3-fold different. On the other hand, S125

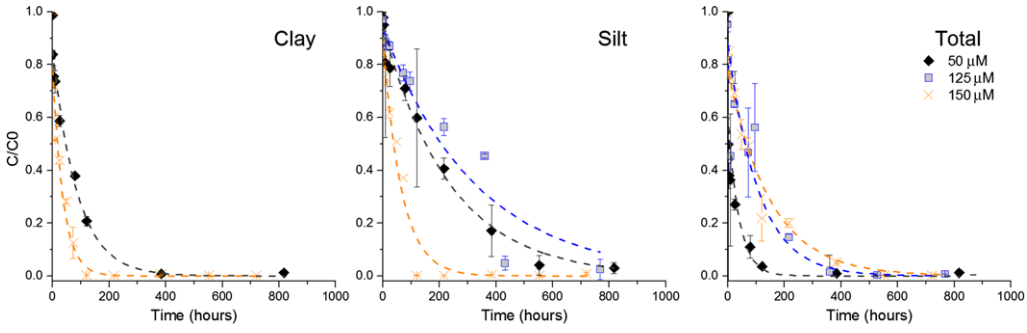

Fig. 3. Time evolution of Se concentrations in solution divided by initial Se concentration plotted for experiments with clay-size fraction (left), silt-size fraction (middle) and Total BC sample (right). Error bars represent the range of duplicate experiments. Different markers represent experiments with different initial Se concentrations. Experimental conditions: pH ~8, $I \approx 0.35$ M and a solid to liquid ratio 50 g l^{-1}. Results from kinetic model M2 are presented as dashed lines.

and S150 have more similar initial Se concentrations but have very different consumption rates. The amount of particles in the <8 µm size fraction was almost twice as high in S150 as in S50. The higher surface area of S150, and possibly larger amount of clay minerals, can explain why Se_{aq} removal was faster than in the experiment with S50. Although less pronounced, the difference in kinetics between the two clay fraction samples and also between the Total samples appears to be related to a higher clay mineral content. The influence of pyrite content on the kinetics of selenite consumption appears to be limited, as can be observed from the similar kinetic behaviours of samples T125 and T150, which have very different pyrite contents.

Speciation of solid-bound Se through time

In order to better constrain the contributions of adsorption and reduction to the removal of Se_{aq}, the speciation of the solid-bound Se was investigated by analysing its XANES and extended EXAFS of its X-ray absorption spectra. XANES analysis revealed a progressing reduction of selenite. That is, the peak at 12 656 eV, which is characteristic for adsorbed selenite, decreased as the peak at 12 652.5 eV, characteristic for red Se^0, increased (Fig. 4). In the EXAFS spectra, the reduction of selenite is reflected by a diminishing contribution of the Se–O scattering path, dominating the EXAFS spectrum of adsorbed selenite, which is replaced by Se–Se scattering in

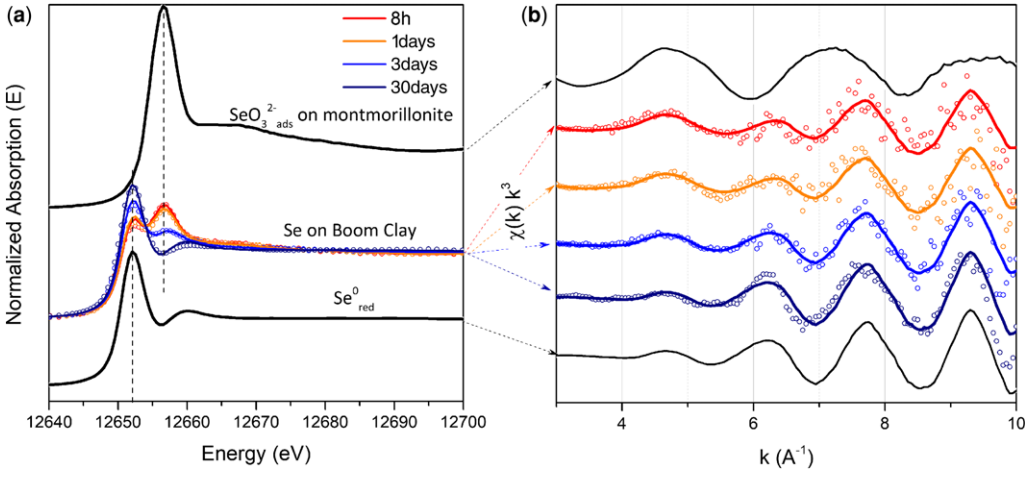

Fig. 4. Selenium K-edge XANES (**a**) and EXAFS (**b**) spectra of Se on BC samples (T150) reacted for different time periods and of two standards, selenite adsorbed on montmorillonite and Se^0_{red}. Circles represent measured data, solid lines represent the results of the linear combination of the spectra from the two standards.

elemental selenium. The corresponding contribution to the EXAFS spectrum is characterized by oscillations of higher frequencies and a maximum amplitude at higher *k*-values compared with the first shell Se–O scatting path. The EXAFS spectrum of Se after reaction with the Total sample can be explained by Se–Se scattering paths with lengths and coordination numbers which are typical for Se^0 bound in Se_8 rings. The EXAFS spectra of samples containing adsorbed selenite are dominated by the resonance features of the three oxygen atoms surrounding the Se in selenite at a distance that has been previously reported for selenite adsorbed onto montmorillonite (Peak *et al.* 2006; see Supplementary Material for details of EXAFS fitting).

All XANES and EXAFS spectra could be reproduced very well by linear combination fitting using two standards, selenite adsorbed onto montmorillonite (Se^{IV}_{ads}) and red elemental Se (Se^0). The corresponding fractions for Se^0 and Se^{IV}_{ads} obtained from EXAFS and from XANES spectra were similar (Supplementary Material, S.4, Table S.2). The results from linear combination fitting are in agreement with those obtained by a more elaborated analysis, combining component analysis, varimax rotation and iterative target testing (Supplementary Material, S.4, Table S.2).

Relative concentrations of solid-bound Se^0_{red} and Se^{IV}_{ads} and the distribution of Se^0_{red} and Se^{IV}_{ads} relative to Se_{tot} at different reaction times are presented in Figure 5. For Clay and Total, initially (at 1.5 h) *c.* 60% of the solid-bound Se was in the form of Se^{IV}_{ads}. For the silt-size fraction, the percentage of Se^{IV}_{ads} was much lower, namely 40%. Through time the relative Se^0_{red} concentrations increased while the relative Se^{IV}_{ads} concentrations decreased. After 30 days, 98% of solid-bound Se was present as Se^0_{red} in all investigated samples and only 1.8% as Se^{IV}_{ads}. These results support the interpretation of the Se_{aq} dynamics that the initial fast removal of Se_{aq} in contact with Clay and Total (Fig. 3) can be predominantly attributed to adsorption of Se^{IV}. Although the relative concentrations of Se^{IV}_{ads} decreased with time, the absolute concentrations of Se^{IV}_{ads} increased in the first 1.5 h, after which they remained approximately constant up to about 24–72 h and decreased afterwards. This implies that after fast, initial adsorption the increase in solid-bound selenium was dominated by reduction of selenite to Se^0 while the pool of

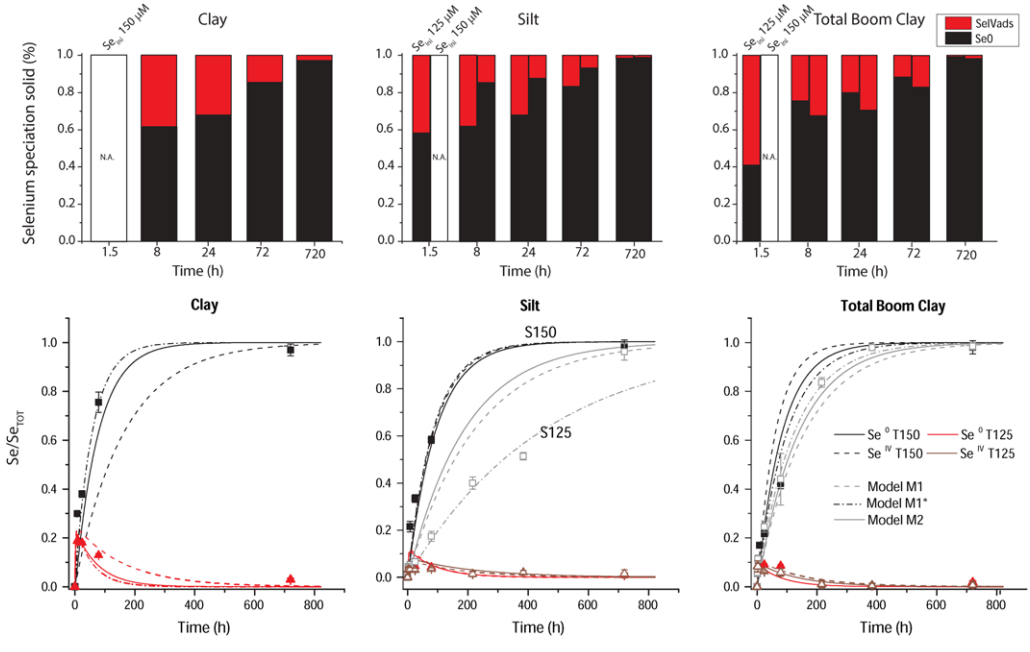

Fig. 5. Top: relative amounts of solid-bound Se species, Se^{IV}_{ads} (red bar) and Se^0 (black bar), in the clay, silt and total sediment sample (C150, S125, S150, T125 and T150) at different time steps. Bottom: time evolution of solid Se (Se/Se_{tot}) species, Se^{IV}_{ads} (red triangles) and Se^0 (black squares). Samples with Se_{tot} 125 μM are represented by open markers and with Se_{tot} 150 μM by closed markers. The lines represent the results from the kinetic model (M1, adsorption by clay minerals and reduction by pyrite; M1*, same as M1 but with k_2 fixed and the surface area of pyrite fitted; M2, adsorption by clay minerals and reduction by pyrite and by clay minerals).

Se^{IV}_{ads} remained practically at a constant level. However, towards the end of the experiment when Se_{aq} had largely been consumed, Se^{IV}_{ads} also vanished and eventually ended up as Se^0 in all experiments.

The quality of the EXAFS spectra is insufficient to unravel the detailed coordination environment of Se^{IV}_{ads} beyond the first oxygen shell. Hence, neither the sorbent nor the specific mechanism for selenite adsorption in these BC samples could be discerned from the spectroscopic results. Furthermore, reduction of selenite by pyrite is considered to be preceded by adsorption of selenite which is then followed by electron transfer reactions, ultimately leading to the formation of Se^0_{red}, grey Se^0 or $FeSe_2$ (Bruggeman *et al.* 2005; Kang *et al.* 2011, 2013; Curti *et al.* 2013). Consequently, selenite adsorbed onto pyrite might account for a part of Se^{IV}_{ads}. For BC, the amount of clay minerals in Clay, Silt and Total samples is much higher (>10 times) than that of pyrite. Furthermore, the reactive surface area is probably higher for the clay minerals than for the pyrite particles; the surface areas of edge sites of various clay minerals range between 5 and 30 $m^2\ g^{-1}$ (Metz *et al.* 2005; Sayed Hassan *et al.* 2006; Macht *et al.* 2011), while the surface areas of pyrite particles range between 2.3 and 4 $m^2\ g^{-1}$ for the smallest framboids <12.5 μm (Pugh *et al.* 1981; Wei & Osseo-Asare 1997). This suggests that selenite adsorption on clay minerals is probably dominating Se^{IV}_{ads}. This assumption is supported by Se^{IV}_{ads} and Se^0 concentrations for Total, T125 and T150 (Supplementary Material, Table S.3). These have very similar Se^{IV}_{ads} concentrations at each measured time step, coinciding with their very similar clay mineral contents, whereas their pyrite content varies by a factor 3. The higher Se^{IV}_{ads} concentrations in Clay compared with Silt and Total also supports the conclusion that most of the Se^{IV}_{ads} is bound to clay minerals.

When assuming that all Se_{aq} is in the form of Se^{IV} the concentration of dissolved Se^{IV} can be used in combination with the contents of Se^{IV}_{ads} to calculate and monitor apparent K_d values for selenite throughout the course of the experiments. After a reaction time of 3.5 h, the apparent K_d values for selenite stayed virtually constant until almost all solid-bound selenium (<3.5% Se_{tot}) had been reduced and the uncertainty of determining Se^{IV}_{ads} concentrations became large. This indicates that sorption processes are fast enough to maintain equilibrium despite the perturbation of the equilibrium owing to removal of Se^{IV} by reduction. When normalizing the apparent K_d values to the clay content, comparable values of *c.* 6.5 ml g^{-1} were obtained for the various experiments despite different Se_{tot} concentrations and clay mineral contents (Supplementary Material, Fig. S.6). The latter further confirms that clay minerals are the dominant sorbent for selenite. This K_d value is low compared with reported K_d values for selenite adsorption on standard (oxic) clay minerals (100–200 ml g^{-1}, e.g. Missana *et al.* 2009). Studies have shown that, upon reduction, the properties of clay minerals, such as surface area and CEC, can change dramatically (Stucki *et al.* 1984; Kostka *et al.* 1999). In reduced clay minerals, a lower specific surface area and a higher surface charge density were observed, which may explain the observed lower affinity of selenite to the clay minerals in BC. Furthermore, it might be possible that part of the selenite adsorbed on clay minerals is directly reduced to Se^0 (see next paragraph). However, if pyrite is the main reductant for selenite, the partial adsorption equilibrium implies that desorption is fast enough to keep up with reduction of selenite by replenishing the pool of dissolved selenite for reaction with pyrite. This, in turn, means that adsorption of selenite on clay minerals does not significantly interfere with reduction of selenite by pyrite. In order to quantitatively elucidate the interplay of adsorption and reduction, the kinetic model was developed.

Kinetic model of selenite interaction with BC

The results from fitting the kinetic model to the observed data are shown in Figure 5 and the corresponding rate constants are listed in Table 2. Input parameters for Clay, Silt and Total samples are presented in the Supplementary Material (Table S.4). The sensitivity analysis showed that in the first 20 h k_1 and k_{-1} are most influential on the Se_{aq} concentrations and that parameter k_2 takes over after 40 h. Sensitivity curves of k_2 and k_3 are very similar, which indicates that it is hard to distinguish the two reduction processes.

The kinetic model, M1, which includes adsorption and desorption of selenite on clay minerals and reduction of selenite to Se^0 by pyrite is able to reproduce the time evolution of Se^{IV}_{ads} in all experiments. Se^0 production is reproduced well in experiments with S150 and Total but is underestimated for experiments with Clay fraction samples with rates being 2-fold lower. To evaluate the fitted rate constants we compared them with rate constants from experiments with selenite and individual clay minerals and pyrite. These were not directly available from the literature, but could be obtained by fitting literature data from selenite experiments with clay minerals and with pyrite using integrated versions of equations (1) and (2) (Supplementary Material, S.6), respectively (clay minerals – Bar-Yosef & Meek 1987; Bruggeman 2006; Missana *et al.* 2009; and pyrite – Bruggeman *et al.* 2005; Kang *et al.* 2011; see Supplementary Material S.7).

The values for k_1 and k_{-1} obtained from our experiments with BC for Se^{IV} adsorption (0.0002 h^{-1} L m^{-2} and 0.3 h^{-1}) lie within the range of derived k_1 and k_{-1} values of Se^{IV} adsorption on clay minerals

Table 2. *Rate constants obtained by fitting data of aqueous Se^{IV} removal due to sorption to clay minerals (top of table) and pyrite (middle of table) using equation (1) and (2) respectively. k′1 is the fitted, conditional, pseudo first-order rate constant which has been converted in to k_1 and k_{-1} based on the equilibrium distribution coefficient, K_d, and the properties of the solids. In the bottom part of the table the rate constants obtained by fitting the kinetic model (equation (1), (2) and (3)) for Se^{IV} adsorption to and reduction by Boom Clay are displayed*

Mineral	Solid/solution ($g\ l^{-1}$)	Se_{tot} ($mol\ l^{-1}$)	A ($m^2\ l^{-1}$)	k_1' (h^{-1})	k_1 (10^{-3} L h^{-1} m^{-2})	k_{-1} (h^{-1})	K_d ($ml\ g^{-1}$)	k_2 (10^{-3} L h^{-1} m^{-2})	k_3 (h^{-1})	R^2
Clay minerals										
Illite du Puy*	3	4E–8	17–89	0.06	0.7–3.6	0.19	105†			0.98
Illite du Puy‡	0.5	1E–8	2.8–15	0.08	5.6–29.2	1.26	130			0.88
Fithian Illite (this study)	15.5	5E–5	87–457	0.8	1.7–9.2	0.24	215			0.85
Smecite FEBEX‡	0.5	1E–8	2.5–7.5	0.02	2.6–8.1	0.19	212			0.68
Smectite SWa-1 (this study)	26.8	5E–5	131–402	0.11	0.3–0.8	0.02	195			0.77
Smectite SWa-1, reduced (this study)	15	5E–5	74–225	0.02	0.09–0.3	0.03	39			0.72
Kaolinite Georgia§	10	1.6E–6	25–63	0.2	3.2–8.0	0.07	285			0.86
Pyrite										
Bruggeman *et al.* (2005)	2.5	5E–6	2.2					0.28		0.94
Bruggeman *et al.* (2005)	2.5	1E–6	2.2					0.67		0.95
Bruggeman *et al.* (2005)	10	5E–6	8.8					0.68		0.96
Bruggeman *et al.* (2005)	10	1E–6	8.8					2.6		0.93
Kang *et al.* (2011)	7.5	1.35E–3	0.83					0.29		0.53
Kang *et al.* (2011)	7.5	4.48E–3	0.83					0.78		0.96
Boom Clay			**SA_{pyr}[$m^2\ g^{-1}$]**							
M1	50	5E–5	C:4, S:2.3 T:2.3		0. 2	0.3	7.14	5.3		0.85
M1* (fixed k_2, fit SA)	50	5E–5	C:23, S125| S150:2.3|4.6 T125|T150:6|3		0. 2	0.3	7.14	2.6		0.96
M2	50	5E–5	C:4, S:2.3 T:2.3		0. 2	0.3	7.14	2.4	0.042	0.93

*Bruggeman (2006).
†The selenite adsorption onto Illite du Puy by Bruggeman (2006) consisted of two phases, adsorption and possibly occlusion. Here, the k-values and the K_d are calculated for the first, fast phase.
‡Missana *et al.* (2009).
§Bar-Yosef & Meek (1987).

(Table 2). The k_2 value, however, is about 8 times larger than the average k_2 value derived from selenite reduction experiments with pure pyrite. One reason for this deviation could be that the specific surface area of pyrite in the BC samples was underestimated, leading to an overestimation of k_2 values. When using the highest k_2 value obtained from literature data and fitting the surface area (M1*), the following optimized surface areas were obtained: 4.2 $m^2\ g^{-1}$ for pyrite in Total; 4.9 $m^2\ g^{-1}$ for pyrite in Silt fraction samples; and 21 $m^2\ g^{-1}$ for pyrite in Clay fraction samples. Using this procedure led to a better agreement between the modelled and determined Se^0 concentrations. The fitted pyrite surface area in Clay is comparable with the BET surface area of microwave synthesized pyrite (15.9 $m^2\ g^{-1}$ (Kim & Batchelor 2009) but by far exceeds the specific surface area of 4 $m^2\ g^{-1}$ reported for both framboidal pyrite of 2–5 μm and pyrite microcrystalites of 1.5 μm (Pugh *et al.* 1981; Wei & Osseo-Asare 1997), which are typical sizes and forms of pyrite observed in the SEM micrographs of our BC samples (Supplementary Material, Fig. S.3)

Direct reduction of Se^{IV} by reduced clay minerals as a parallel pathway for Se^0 production in BC provides an alternative explanation for the faster reduction of Se^{IV} than expected based on the content and properties of pyrite and reported reduction kinetics. The possibility of Se^{IV} reduction by adsorbed Fe^{II} on clay minerals has been reported (Charlet *et al.* 2007) and reduction of Cr^{VI} and Tc^{VII} by reduced clay minerals has been demonstrated (Peretyazhko *et al.* 2009; Taylor *et al.* 2000; Yang *et al.* 2012; Bishop *et al.* 2014). This could also be an explanation for the low K_d values found for clay minerals in BC, with adsorbed Se^{IV} constantly being reduced to Se^0. The electron donating capacity of clay minerals/natural organic matter in BC, measured by mediated electrochemistry, is *c.* 40 μmol $e^-\ g^{-1}$ (Hoving *et al.* 2017), which exceeds the required electron donating capacity for reducing all Se^{IV} to Se^0 by 10–40 times. An extended model including a first-order reduction term for Se^{IV}_{ads} (Model M2 Fig. 5, solid line) was able to reproduce the kinetics of Se^{IV} reduction in all experiment with k_2 value and pyrite surface area in the expected ranges. In this scenario, reduction by clay minerals accounted for about 40% (Total and Silt) to 90% (Clay) of Se^0 production. However, additional experiments with isolated, reduced clay minerals are necessary to confirm that Se^{IV} reduction by structurally bound Fe^{II} in clay minerals occurs within the time frame of these experiments. In any case, the capability of the models M1* and M2 to reproduce the measured trends in experiments with different initial concentrations supports the adequacy of the kinetic model by conceiving adsorption and reduction as first order with respect of dissolved selenite.

Conclusions

Irrespective of whether or not reduction of selenite by clay minerals contributes to the Se^0 reduction, our results demonstrate that adsorption of selenite to clay minerals does not prevent quantitative reduction of selenite within the timescale of the experiments. In case that pyrite is the dominant reductant for selenite, desorption of selenite adsorbed to clay minerals is fast enough to replenish the pool of dissolved selenite, a prerequisite for the reaction with pyrite. The main final product is Se^0 which means that in the long term, solubility of Se^0 will likely constrain Se mobility. The reductive capacity of clay sediments for selenite might be higher than anticipated when based on pyrite alone, due to the potential pathway of selenite reduction by reduced clay minerals. The adsorptive capacity for reduced clays may however be overestimated when literature K_d-values, based on selenite adsorption onto oxic clay minerals, are used.

Supporting information

X-ray diffractograms of separated clay-size, silt-size and total BC material are available as supplementary information. Also provided are particle size distributions of all materials and extra information on XANES and EXAFS results, Se concentrations through time for experiments with standard clay minerals and figures of the sensitivity analysis of the kinetic model.

Acknowledgments The manuscript was written through the contributions of all authors. M.A.M and A.L.H. performed and analysed the experiments, D.B. helped collect and analyse the X-ray absorption spectroscopy and C.B., T.B. and A.L.H wrote the manuscript. All authors have given approval to the final version of the manuscript. We also thank the staff of the ESRF and the DUBBLE beamline, in particular, for their support. We would also like to thank Joan Govaerts for his contribution to the sensitivity analysis.

Funding The research leading to these results has received funding from the Dutch research programme on geological disposal OPERA. OPERA is financed by the Dutch Ministry of Economic Affairs and the public limited liability company Elektriciteits-Produktiemaatschappij Zuid-Nederland and coordinated by the The Central Organization for Radioactive Waste. The XAS measurements were funded by the Netherlands Organization for Scientific Research (NWO).

References

Aerts, S., Jacops, S. & Dewel, A. 2008. *Microbial Activity around the Connecting Gallery*. External Report **SCK•CEN-ER-61**.

Badaut, V., Schlegel, M.L., Descostes, M. & Moutiers, G. 2012. *In situ* time-resolved X-ray near-edge absorption spectroscopy of selenite reduction by siderite. *Environmental Science and Technology*, **46**, 10820–10826, https://doi.org/10.1021/es301611e

Bar-Yosef, B. 1987. Selenium desorption from Ca–kaolinite. *Communications in Soil Sience and Plant Analysis*, **18**, 771–779, https://doi.org/10.1080/00103628709367860

Bar-Yosef, B. & Meek, D. 1987. Selenium sorption by kaolinite and montmorillonite. *Soil Science*, **144**, 11–19, https://doi.org/10.1097/00010694-198707000-00003

Beauwens, T., De Canniere, P., Moors, H., Wang, L. & Maes, N. 2005. Studying the migration behaviour of selenate in Boom Clay by electromigration. *Engineering Geology*, **77**, 285–293, https://doi.org/10.1016/j.enggeo.2004.07.019

Behrends, T., van der Veen, I., Hoving, A. & Griffioen, J. 2016. First assessment of the pore water composition of Rupel Clay in the Netherlands and the characterisation of its reactive solids. *Netherlands Journal of Geosciences*, **95**, 315–335, https://doi.org/10.1017/njg.2016.23

Bergaya, F., Lagaly, G. & Vayer, M. 2006. Cation and anion exchange. *In*: Bergaya, F., Theng, B.K.G. & Lagaly, G. (eds) *Handbook of Clay Science*, Elservier, Amsterdam, 979–1001, https://doi.org/10.1016/S1572-4352(05)01036-6

Bishop, M.E., Glasser, P., Dong, H., Arey, B. & Kovarik, L. 2014. Reduction and immobilization of hexavalent chromium by microbially reduced Fe-bearing clay minerals. *Geochimica et Cosmochimica Acta*, **133**, 186–203, https://doi.org/10.1016/j.gca.2014.02.040

Boivin-Jahns, V., Ruimy, R., Bianchi, A., Daumas, S. & Christen, R. 1996. Bacterial diversity in a deep-subsurface clay environment. *Applied and Environmental Microbiology*, **62**, 3405–3412.

Borsboom, M., Bras, W. *et al.* 1998. The Dutch–Belgian beamline at the ESRF. *Journal of Synchrotron Radiation*, **5**, 518–520, https://doi.org/10.1107/S0909049597013484

Breynaert, E., Bruggeman, C. & Maes, A. 2008. XANES-EXAFS analysis of se solid-phase reaction products formed upon contacting Se(IV) with FeS_2 and FeS. *Environmental Science and Technology*, **42**, 3595–3601, https://doi.org/10.1021/es071370r

Breynaert, E., Scheinost, A.C. *et al.* 2010. Reduction of Se(IV) in boom clay: XAS solid phase speciation. *Environmental Science & Technology*, **44**, 6649–6655, https://doi.org/10.1021/es100569e

Bruggeman, C. 2006. *Assessment of the geochemical behaviour of selenium oxyanions under boom clay geochemical conditions*. Katholieke Universiteit Leuven.

Bruggeman, C. & Maes, N. 2010. Uptake of uranium(VI) by pyrite under boom clay conditions: influence of dissolved organic carbon. *Environmental Science & Technology*, **44**, 4210–4216, https://doi.org/10.1021/es100919p

Bruggeman, C., Maes, A., Vancluysen, J. & Vandemussele, P. 2005. Selenite reduction in Boom clay: effect of FeS_2, clay minerals and dissolved organic matter. *Environmental Pollution (Barking, Essex: 1987)*, **137**, 209–221, https://doi.org/10.1016/j.envpol.2005.02.010

Chao, T.T. & Sanzolone, R.F. 1989. Fractionation of soil selenium by sequential partial dissolution. *Soil Science Society of America Journal*, **53**, 385–380, https://doi.org/10.2136/sssaj1989.03615995005300020012x

Charlet, L., Scheinost, A.C. *et al.* 2007. Electron transfer at the mineral/water interface: selenium reduction by ferrous iron sorbed on clay. *Geochimica et Cosmochimica Acta*, **71**, 5731–5749, https://doi.org/10.1016/j.gca.2007.08.024

Charlet, L., Kang, M., Bardelli, F., Kirsch, R., Géhin, A., Grenèche, J.-M. & Chen, F. 2012. Nanocomposite pyrite-greigite reactivity toward Se(IV)/Se(VI). *Environmental Science & Technology*, **46**, 4869–4876, https://doi.org/10.1021/es204181q

Claff, S.R., Sullivan, L.A., Burton, E.D. & Bush, R.T. 2010. A sequential extraction procedure for acid sulfate soils: partitioning of iron. *Geoderma*, **155**, 224–230, https://doi.org/10.1016/j.geoderma.2009.12.002

Curti, E., Aimoz, L. & Kitamura, A. 2013. Selenium uptake onto natural pyrite. *Journal of Radioanalytical and Nuclear Chemistry*, **295**, 1655–1665, https://doi.org/10.1007/s10967-012-1966-9

De Cannière, P., Maes, A., Williams, S., Bruggeman, C., Beauwens, T., Maes, N. & Cowper, M. 2010. *Behaviour of Selenium in Boom Clay*. State-of-the-Art Report.

De Craen, M., Swennen, R. & Keppens, E. 1998. Petrography and geochemistry of septarian carbonate concretions from the Boom Clay Formation (Oligocene, Belgium). *Geologie en Mijnbouw*, **77**, 63–76, https://doi.org/:10.1023/A:1003468328212

De Craen, M., Wang, L., Van Geet, M. & Moors, H. 2004. *Geochemistry of Boom Clay Pore Water at the Mol Site – Status 2004*, Scientific Report **BLG-990**. Mol, Belgium.

Delécaut, G. 2004. *The geochemical behaviour of uranium in the Boom Clay*. PhD dissertation, Katholieke Universiteit Leuven, Louvain-La-Neuve Belgium.

Dhillon, K.S. & Dhillon, S.K. 1999. Adsorption-desorption reactions of selenium in some soils of India. *Geoderma*, **93**, 19–31, https://doi.org/10.1016/S0016-7061(99)00040-3

Ervanne, H., Hakanen, M. & Lehto, J. 2016. Selenium sorption on clays in synthetic groundwaters representing crystalline bedrock conditions. *Journal of Radioanalytical and Nuclear Chemistry*, **307**, 1365–1373, https://doi.org/10.1007/s10967-015-4254-7

Goldberg, S. 2013. Modeling selenite adsorption envelopes on oxides, clay minerals, and soils using the triple layer model. *Soil Science Society of America Journal*, **77**, 64–71, https://doi.org/10.2136/sssaj2012.0205

Goldberg, S. & Glaubig, R.A. 1988. Anion sorption on a calcareous, Montmorillonitic soil-selenium. *Soil Sci. Soc. Am. J.*, **52**, 954–958, https://doi.org/10.2136/sssaj1988.03615995005200040010x

Hamilton, S.J. 2004. Review of selenium toxicity in the aquatic food chain. *Science of the Total Environment*, **326**, 1–31, https://doi.org/10.1016/j.scitotenv.2004.01.019

Hoving, A.L., Sander, M., Bruggeman, C. & Behrends, T. 2017. Redox properties of clay-rich sediments as assessed by mediated electrochemical analysis: separating pyrite, siderite and structural Fe in clay minerals. *Chemical Geology*, **457**, 149–161, https://doi.org/10.1016/j.chemgeo.2017.03.022

Huo, L., Xie, W., Qian, T., Guan, X. & Zhao, D. 2017. Reductive immobilization of pertechnetate in soil and groundwater using synthetic pyrite nanoparticles. *Chemosphere*, **174**, 456–465, https://doi.org/10.1016/j.chemosphere.2017.02.018

IAEA 2003. *Scientific and Technical Basis for the Geological Disposal of Radioactive Wastes*. International Atomic Energy, Vienna.

Ilton, E.S., Haiduc, A., Moses, C.O., Heald, S.M., Elbert, D.C. & Veblen, D.R. 2004. Heterogeneous reduction of uranyl by micas: crystal chemical and solution controls. *Geochimica et Cosmochimica Acta*, **68**, 2417–2435, https://doi.org/10.1016/j.gca.2003.08.010

Jacops, E., Wouters, K. *et al.* 2015. Measuring the effective diffusion coefficient of dissolved hydrogen in saturated Boom Clay. *Applied Geochemistry*, **61**, 175–184, https://doi.org/10.1016/j.apgeochem.2015.05.022

Jaisi, D.P., Dong, H., Plymale, A.E., Fredrickson, J.K., Zachara, J.M., Heald, S. & Liu, C. 2009. Reduction and long-term immobilization of technetium by Fe(II) associated with clay mineral nontronite. *Chemical Geology*, **264**, 127–138, https://doi.org/10.1016/j.chemgeo.2009.02.018

Jörg, G., Bühnemann, R., Hollas, S., Kivel, N., Kossert, K., Van Winckel, S. & Lierse von Gostomski, C. 2010. Preparation of radiochemically pure ^{79}Se and highly precise determination of its half-life. *Applied Radiation and Isotopes*, **68**, 2339–2351, https://doi.org/10.1016/j.apradiso.2010.05.006

Kang, M., Chen, F., Wu, S., Yang, Y., Bruggeman, C. & Charlet, L. 2011. Effect of pH on aqueous Se(IV) reduction by pyrite. *Environmental Science & Technology*, **45**, 2704–2710, https://doi.org/10.1021/es1033553

Kang, M., Ma, B. *et al.* 2013. Interaction of aqueous Se (IV)/Se(VI) with FeSe/$FeSe_2$: implication to Se redox process. *Journal of Hazardous Materials*, **248–249**, 20–28, https://doi.org/10.1016/j.jhazmat.2012.12.037

Kim, E.J. & Batchelor, B. 2009. Synthesis and characterization of pyrite (FeS_2) using microwave irradiation. *Materials Research* Bulletin, **44**, 1553–1558, https://doi.org/10.1016/j.materresbull.2009.02.006

Koenen, M. & Griffioen, J. 2016. Characterisation of the geochemical heterogeneity of the Rupel Clay Member in the Netherlands. *Netherlands Journal of Geosciences*, **95**, 269–281, https://doi.org/10.1017/njg.2016.6

Konert, M. & Vandenberghe, J. 1997. Comparison of laser grain size analysis with pipette and sieve analysis: a solution for the underestimation of the clay fraction. *Sedimentology*, **44**, 523–535, https://doi.org/10.1046/j.1365-3091.1997.d01-38.x

Kostka, J., Wu, J., Nealson, K. & Stucki, J. 1999. The impact of structural Fe (III) reduction by bacteria on the surface chemistry of smectite clay minerals. *Geochimica et Cosmochimica Acta*, **63**, 3705–3713, https://doi.org/10.1016/S0016-7037(99)00199-4

Liu, Y., Terry, J. & Jurisson, S. 2008. Pertechnetate immobilization with amorphous iron sulfide. *Radiochimica Acta*, **96**, 823–833, https://doi.org/10.1524/ract.2008.1528

Macht, F., Eusterhues, K., Pronk, G.J. & Totsche, K.U. 2011. Specific surface area of clay minerals: comparison between atomic force microscopy measurements and bulk-gas (N_2) and -liquid (EGME) adsorption methods. *Applied Clay Science*, **53**, 20–26, https://doi.org/10.1016/j.clay.2011.04.006

Maes, N., Moors, H., Wang, L., Delècaut, G., De Canniere, P. & Put, M. 2002. The use of electromigration as a qualitative technique to study the migration behaviour and speciation of uranium in the Boom Clay. *Radiochimica Acta*, **90**, 741–746, https://doi.org/10.1524/ract.2002.90.9-11_2002.741

Metz, V., Raanan, H., Pieper, H., Bosbach, D. & Ganor, J. 2005. Towards the establishment of a reliable proxy for the reactive surface area of smectite. *Geochimica et Cosmochimica Acta*, **69**, 2581–2591, https://doi.org/10.1016/j.gca.2004.11.009

Missana, T., Alonso, U. & García-Gutiérrez, M. 2009. Experimental study and modelling of selenite sorption onto illite and smectite clays. *Journal of Colloid and Interface Science*, **334**, 132–138, https://doi.org/10.1016/j.jcis.2009.02.059

Nikitenko, S., Beale, A.M. *et al.* 2008. Implementation of a combined SAXS/WAXS/QEXAFS set-up for time-resolved *in situ* experiments. *Journal of Synchrotron Radiation*, **15**, 632–640, https://doi.org/10.1107/S0909049508023327

OPERA, Verhoef, E. & Schroeder, T. 2011. Research Plan. OPERA-PG-COV004.

Ortiz, L., Volckaert, G. & Mallants, D. 2002. Gas generation and migration in Boom Clay, a potential host rock formation for nuclear waste storage. *Engineering Geology*, **64**, 287–296, https://doi.org/10.1016/S0013-7952(01)00107-7

Peak, D., Saha, U. & Huang, P. 2006. Selenite adsorption mechanisms on pure and coated montmorillonite: an EXAFS and XANES spectroscopic study. *Soil Science Society of America Journal*, **70**, 192, https://doi.org/10.2136/sssaj2005.0054

Peretyazhko, T., Zachara, J.M. *et al.* 2009. Heterogeneous reduction of Tc (VII) by Fe (II) at the solid–water interface. *Geochimica et Cosmochimica Acta*, **72**, 1521–1539, https://doi.org/10.1016/j.gca.2008.01.004

PTB-Physikalisch-Technische-Bundesanstalt. 2010. The half-life of ^{79}Se. 1–2.

Pugh, C.E., Hossner, L.R. & Dixon, J.B. 1981. Pyrite and marcasite surface area as influenced by morphology and particle diameter. *Soil Science Society of America Journal*, **45**, 979, https://doi.org/10.2136/sssaj1981.03615995004500050033x

Ramaswamy, V. & Rao, P.S. 2006. Grain size analysis of sediments from the Northern Andaman Sea: comparison of laser diffraction and Sieve-Pipette techniques. *Journal of Coastal Research*, **224**, 1000–1009, https://doi.org/10.2112/04-0162.1

Ravel, B. & Newville, M. 2005. ATHENA, ARTEMIS, HEPHAESTUS: data analysis for X-ray absorption spectroscopy using IFEFFIT. *Journal of synchrotron radiation*, **12**, 237–541.

Reitz, A., Pfeifer, K., De Lange, G.J. & Klump, J. 2004. Biogenic barium and the detrital Ba/Al ratio: a comparison of their direct and indirect determination. *Marine Geology*, **204**, 289–300, https://doi.org/10.1016/S0025-3227(04)00004-0

Rempe, N.T. 2007. Permanent underground repositories for radioactive waste. *Progress in Nuclear Energy*,

49, 365–374, https://doi.org/10.1016/j.pnucene.2007.04.002

Sayed Hassan, M., Villieras, F., Gaboriaud, F. & Razafitianamaharavo, A. 2006. AFM and low-pressure argon adsorption analysis of geometrical properties of phyllosilicates. *Journal of Colloid and Interface Science*, **296**, 614–623, https://doi.org/10.1016/j.jcis.2005.09.028

Scheinost, A.C. & Charlet, L. 2008. Selenite reduction by mackinawite, magnetite and siderite: XAS characterization of nanosized redox products. *Environmental Science & Technology*, **42**, 1984–1989, https://doi.org/10.1021/es071573f

Scheinost, A.C., Kirsch, R., Banerjee, D., Fernandez-Martinez, A., Zaenker, H., Funke, H. & Charlet, L. 2008. X-ray absorption and photoelectron spectroscopy investigation of selenite reduction by FeII-bearing minerals. *Journal of Contaminant Hydrology*, **102**, 228–245, https://doi.org/10.1016/j.jconhyd.2008.09.018

Stucki, J.W., Golden, D.C. & Roth, C.B. 1984. Effects of reduction and reoxidation of structural Iron on the surface charge and dissolution of dioctahedral smectites. *Clays and Clay Minerals*, **32**, 350–356, https://doi.org/10.1346/CCMN.1984.0320502

Taylor, R.W., Shen, S., Bleam, W.F. & Tu, S.I. 2000. Chromate removal by dithionite-reduced clays: evidence from direct X-ray adsorption near edge spectroscopy (XANES) of chromate reduction at clay surfaces. *Clays and Clay Minerals*, **48**, 648–654, https://doi.org/10.1346/CCMN.2000.0480606

Tsai, S.C., Wang, T.H., Li, M.H., Wei, Y.Y. & Teng, S.P. 2009. Cesium adsorption and distribution onto crushed granite under different physicochemical conditions. *Journal of Hazardous Materials*, **161**, 854–861, https://doi.org/10.1016/j.jhazmat.2008.04.044

Wei, D. & Osseo-Asare, K. 1997. Aqueous synthesis of finely divided pyrite particles. *Colloids and Surfaces A: Physicochemical and Engineering Aspects*, **121**, 27–36, https://doi.org/10.1016/S0927-7757(95)03502-8

Yang, J., Kukkadapu, R.K., Dong, H., Shelobolina, E.S., Zhang, J. & Kim, J. 2012. Effects of redox cycling of iron in nontronite on reduction of technetium. *Chemical Geology*, **291**, 206–216, https://doi.org/10.1016/j.chemgeo.2011.10.013

Yllera De Llano, A., Bidoglio, G., Avogadro, A., Gibson, P.N. & Rivas Romero, P. 1996. Redox reactions and transport of selenium through fractured granite. *Journal of Contaminant Hydrology*, **21**, 129–139, https://doi.org/10.1016/0169-7722(95)00038-0

Zhang, H. & Selim, H.M. 2005. Kinetics of arsenate adsorption-desorption in soils. *Environmental Science & Technology*, **39**, 6101–6108, https://doi.org/10.1021/es050334u